Research Article | Open Access

Soft Science

Song *et al. Soft Sci.* **2026**, *6*, 59 **DOI:**10.20517/ss.2026.64

A flexible multimodal sensor with intrinsic signal decoupling for wearable respiratory monitoring

Ziyang Song[1,2,3], Chen Huang[1], Evgeniya Sheremet[4], Raul D. Rodriguez[4], Liangjing Shi[2], Yin Cheng[2], Jing Sun[2], Guan-E Wang[5,*], Ranran Wang[1,2,*]

Keywords:
Multimodal sensor, self-decoupling, respiration monitoring, flexible sensor, MXene, metal-organic framework

Citation: Song, Z.; Huang, C.; Sheremet, E.; Rodriguez, R. D.; Shi, L.; Cheng, Y.; Sun, J.; Wang, G. E.; Wang, R. A flexible multimodal sensor with intrinsic signal decoupling for wearable respiratory monitoring. *Soft Sci.* **2026**, *6*, 59. https://dx.doi.org/10.20517/ss.2026.64

Received: 31 Mar 2026 **First Decision:** 24 Apr 2026 **Revised:** 8 May 2026 **Accepted:** 22 May 2026 **Published:** 3 Jul 2026

Academic Editor: Mazeyar Parvinzadeh Gashti
Copy Editor: Pei-Yun Wang
Production Editor: Pei-Yun Wang

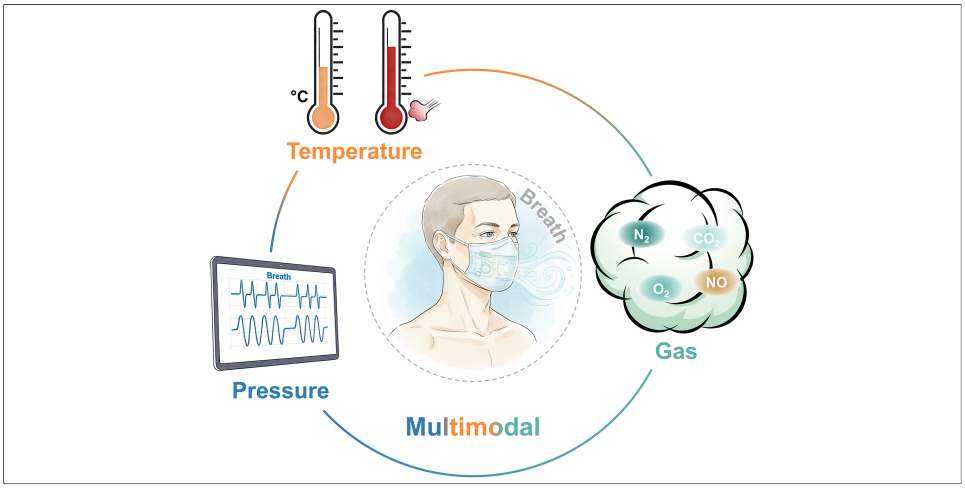

Abstract

Continuous, noninvasive monitoring of multiple physiological signals derived from exhaled breath (EB), is critical for managing respiratory diseases such as asthma and chronic obstructive pulmonary disease (COPD). However, current wearable sensors face fundamental limitations, including signal cross-talk, inadequate multi-parameter detection, and poor mechanical stability. Here, we introduce a flexible multimodal sensor with intrinsic device-level signal decoupling for comprehensive wearable respiratory monitoring. The sensor features a compact vertically stacked architecture that integrates pressure, temperature, and nitric oxide (NO) modules, each isolating signals through orthogonal transduction mechanisms: piezoresistive current, junction potential, and chemiresistive response. The pressure module, based on aerosol-jet-printed MXene ($Ti_3C_2T_x$)/hydroxyethyl cellulose (HEC) films with engineered gradient microstructures,

[1]School of Chemistry and Materials Science, Hangzhou Institute for Advanced Study, University of Chinese Academy of Sciences, Hangzhou 310024, Zhejiang, China.
[2]State Key Laboratory of High Performance Ceramics, Shanghai Institute of Ceramics, Chinese Academy of Sciences, Shanghai 200050, China.
[3]Center of Materials Science and Optoelectronics Engineering, University of Chinese Academy of Sciences, Beijing 100049, China.
[4]Tomsk Polytechnic University, Tomsk 634050, Russia.
[5]State Key Laboratory of Structural Chemistry, Fujian Institute of Research on the Structure of Matter, Chinese Academy of Sciences, Fuzhou 350002, Fujian, China.

***Correspondence to:** Prof. Guan-E Wang, State Key Laboratory of Structural Chemistry, Fujian Institute of Research on the Structure of Matter, Chinese Academy of Sciences, Fuzhou 350002, Fujian, China. E-mail: gewang@fjirsm.ac.cn; Prof. Ranran Wang, State Key Laboratory of High Performance Ceramics, Shanghai Institute of Ceramics, Chinese Academy of Sciences, Shanghai 200050, China. E-mail: wangranran@mail.sic.ac.cn

achieves exceptional sensitivity of 2.75 kPa^{-1} over a broad linear range up to 160 kPa with high linearity ($R^2 > 0.99$). Simultaneously, the temperature module, constructed from an MXene/EtDAB·$4PbI_2$ Schottky-like junction, delivers a remarkable sensitivity of 6.5 $mV·K^{-1}$. For gas detection, an electrochemically exfoliated graphene (EEG)/Co_3(HITP)$_2$ hybrid enables an NO detection limit down to 25 ppb under ambient conditions. In addition, we integrated the sensor into a smart facemask to enable real-time monitoring of respiratory patterns and to distinguish normal and high-fractional exhaled nitric oxide simulated EB, illustrating the potential of this technology for personalized healthcare.

INTRODUCTION

Respiratory diseases, including asthma and chronic obstructive pulmonary disease (COPD), constitute a major global health burden due to their high prevalence, chronic progression, and frequent exacerbations[1-3]. Mounting clinical evidence indicates that disease deterioration is often preceded by subtle yet measurable changes in respiratory patterns and airway inflammatory status, including increased respiratory rate (RR), altered tidal volume, and markers of airway inflammation[4-6]. This recognition is fueling growing demands for continuous, non-invasive, real-time respiratory monitoring technologies, particularly in wearable formats, to enable early warning systems, long-term disease management, and objective therapeutic assessment[7].

From both physiological and pathological perspectives, respiratory disorders are inherently multidimensional phenomena that cannot be adequately described by single-parameter measurements. RR and tidal volume reflect ventilatory load and neuromuscular control[8], while exhaled breath (EB) temperature correlates with airway blood flow and localized inflammation[9]. In addition, the composition of EB, particularly nitric oxide (NO), serves as a well-established biomarker of airway inflammation[10]. Importantly, different respiratory diseases and their stages are characterized by unique combinations and fluctuations of these parameters, rather than isolated abnormalities, highlighting the physiological interdependence of respiratory metrics[11]. This complexity calls for integrating pressure, temperature, and gas-sensing capabilities into a single platform, enabling complementary respiratory signals to collectively provide a more comprehensive and reliable assessment of respiratory health.

So far, researchers have developed a wide range of mono-, dual-, and multifunctional respiratory sensors. Single-function sensors offer limited physiological information and are inherently susceptible to misinterpretation due to their narrow range of detectable data[12-16]. Although dual-functional sensors extend sensing dimensions, they remain insufficient to capture the full complexity of respiratory physiology and often suffer from signal cross-talk between sensing modes[16-19]. Multi-functional sensors provide richer, more comprehensive datasets, but they often require larger sizes, more complex structures, or advanced algorithms for signal decoupling. These methods can introduce additional challenges, including signal cross-talk, data instability, and increased system complexity[20-26]. In wearable applications, these limitations are exacerbated by signal coupling arising from shared stimuli, such as airflow, temperature fluctuations, and mechanical deformation, as well as unavoidable mechanical strain and motion-induced artifacts during daily activities[27]. These factors make accurate parameter extraction and long-term signal stability more difficult. Although structural separation, spatial arrangement, and algorithm-assisted processing have been used to mitigate cross-talk in multimodal sensors, these strategies often suppress or correct coupled signals after stimulus interference has occurred, rather than decoupling the transduction processes at the source. Consequently, achieving intrinsic signal self-decoupling at the device level, rather than relying on post-processing computational separation, remains a critical yet underexplored challenge in flexible multimodal respiratory sensing. Overcoming this challenge requires highly integrated, strain-insensitive wearable sensors with robust intrinsic decoupling capabilities, which are essential for realizing multimodal clinical respiratory monitoring in healthcare applications.

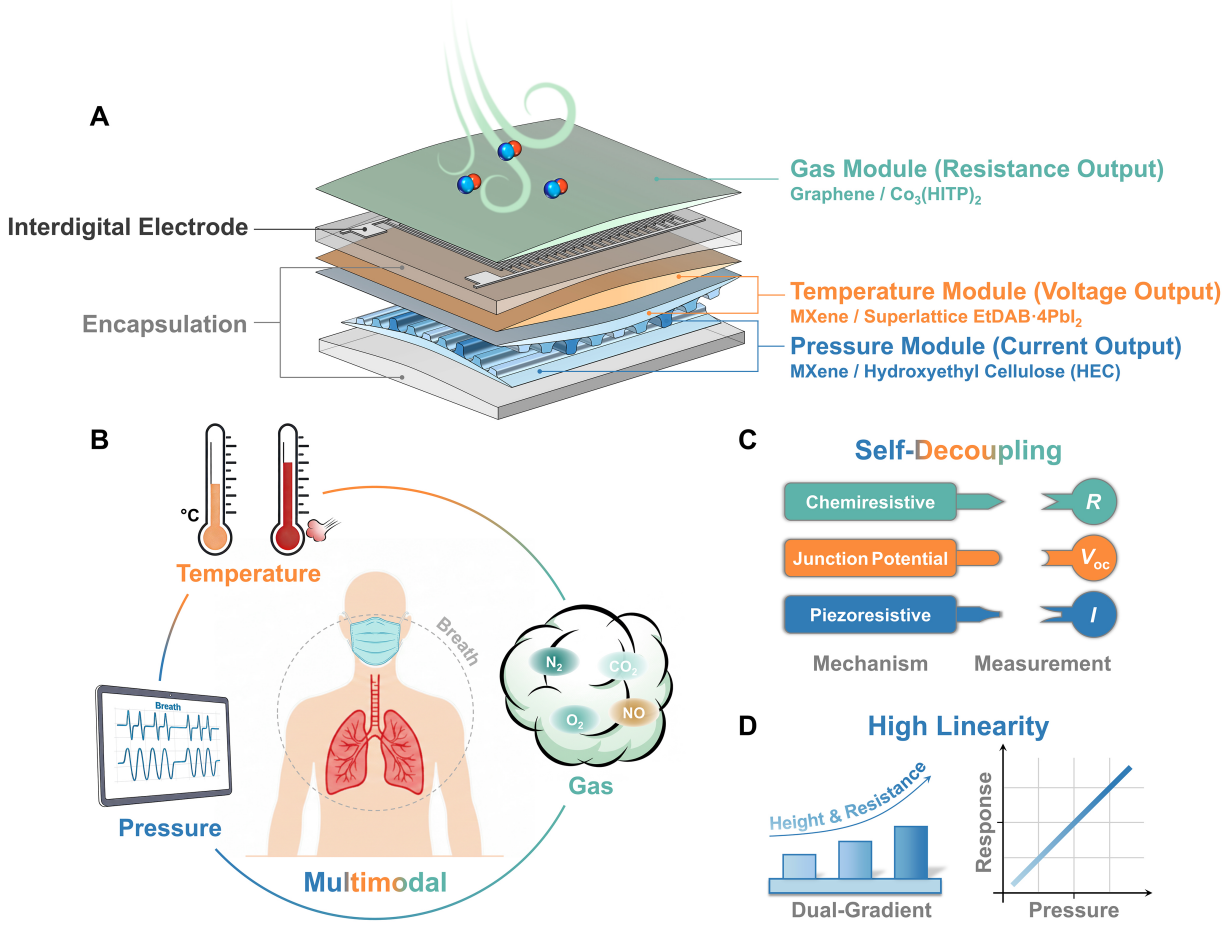

Figure 1. Structural design and working principle of the flexible multimodal sensor. (A) Schematic illustration of the vertically stacked sensor architecture integrating pressure-, temperature-, and gas-sensing modules; (B) Schematic illustration of the multimodal respiratory monitoring capability; (C) Schematic illustration of intrinsic signal self-decoupling; (D) Schematic illustration of the high linearity of the structure–resistance dual-gradient pressure module.

Here, we report a flexible multimodal sensor that integrates pressure, temperature, and NO sensing in a compact vertically stacked architecture, arranged from bottom to top [Figure 1A]. The device consists of three modules, each operating through orthogonal transduction mechanisms: a pressure-sensing module based on piezoresistive current, a temperature-sensing module exploiting junction potential between heterogeneous materials, and a chemiresistive NO gas-sensing module [Figure 1B]. This device strategy with independent readout channels enables intrinsic signal decoupling at the device-physics level, allowing simultaneous and reliable acquisition of multiple respiratory parameters without reliance on complex postprocessing algorithms [Figure 1C]. Unlike multimodal sensing systems that mainly rely on spatial separation, structural isolation, or post-processing algorithms to separate coupled signals, this design converts different respiratory stimuli into intrinsically distinct electrical outputs before signal acquisition. Such device-level decoupling reduces the dependence on complex signal correction while maintaining a compact vertically integrated architecture.

The pressure module utilizes aerosol-jet-printed MXene ($Ti_3C_2T_x$)/hydroxyethyl cellulose (HEC) films, where the excellent electrical conductivity and mechanical flexibility of MXene facilitate efficient stress-to-current transduction [Supplementary Figures 1 and 2]. A structure–resistance dual-gradient design is engineered by modulating stripe height and the MXene/HEC ratio, producing gradient resistance and staged contact that

delivers high sensitivity of 2.75 kPa^{-1} with excellent linearity ($R^2 > 0.99$) over a broad pressure range up to 160 kPa [Figure 1D]. The temperature module is based on a MXene/EtDAB·4PbI_2 Schottky-like junction. The superlattice material EtDAB·4PbI_2 is a *p*-type semiconductor that synergistically combines the mechanical flexibility of EtDAB with the unique band structure of PbI_2 [Supplementary Figures 1 and 3][28]. By monitoring the temperature-dependent change in open-circuit voltage (ΔV_{oc}) across the assembled Schottky-like junction, this design enables real-time temperature sensing with a sensitivity of 6.5 $mV \cdot K^{-1}$. The NO gas detection unit includes a hybrid composite of electrochemically exfoliated graphene (EEG) and the conductive metal–organic framework (MOF) $Co_3(HITP)_2$ (HITP = 2,3,6,7,10,11-hexaiminotriphenylene) [Supplementary Figures 1 and 4], which is coated onto silver interdigital electrodes, and achieves a detection limit of 25 ppb under ambient conditions[29]. To prevent gas-induced interference with pressure and temperature measurements and improve device reliability, the lower two modules are encapsulated in polydimethylsiloxane (PDMS), a flexible and chemically inert elastomer[27]. The vertically integrated configuration minimizes device footprint, while engineering the elastic modulus between layers effectively mitigates strain-induced signal interference, enhancing sensing stability under mechanical deformation. To demonstrate its practical clinical applicability, we integrate the sensor into a flexible smart facemask to track RR and fractional exhaled nitric oxide (FeNO). When combined with pulse monitoring, the system provides a comprehensive assessment of cardiorespiratory health, offering a robust platform for the early detection and monitoring of respiratory inflammatory diseases.

EXPERIMENTAL

Chemicals and materials

Ti_3AlC_2 MAX phase powder was purchased from Forsman Scientific (Beijing) Co., Ltd. Hydrochloric acid (HCl, 36-38 wt%), HEC, lead iodide (PbI_2), N,N-dimethylformamide (DMF, 99.8%), cobalt(II) nitrate hexahydrate [$Co(NO_3)_2 \cdot 6H_2O$], 2,3,6,7,10,11-hexaminotriphenylene hexahydrochloride (HATP·6HCl), methanol, and nylon membranes were purchased from Shanghai Titan Scientific Co., Ltd. Lithium fluoride (LiF) and sodium acetate (NaOAc) were purchased from Sinopharm Chemical Reagent Co., Ltd. Mixed cellulose filter membranes were purchased from Merck Millipore, USA. PDMS (Sylgard 184) was purchased from Dow Corning (China) Co., Ltd. N,N,N′,N′-tetraethylbenzidine[28,30] [EtDAB, 4,4′-bis(diethylamino)biphenyl] and EEG[31] were provided by collaborating laboratories. Deionized water (DI) was produced in the laboratory.

Synthesis of MXene ($Ti_3C_2T_x$)

LiF (1.5 g) was dissolved in 20 mL of 9 m HCl and stirred at 600 rpm for 15 min at room temperature (RT), followed by the slow addition of Ti_3AlC_2 (1 g). The mixture was etched at 35 °C for 24 h. The product was washed with DI via centrifugation at 4,000 rpm for 5 min per cycle until pH of the supernatant was above 6, and then freeze-dried to obtain multilayer $Ti_3C_2T_x$. Delamination was achieved by sonication in water for 1 h, followed by centrifugation (3,500 rpm, 30 min). The supernatant was collected and freeze-dried to yield single-layer $Ti_3C_2T_x$.

Preparation of MXene films

The obtained MXene powder was dispersed in DI and oscillated to form a homogeneous dispersion (10 $mg \cdot mL^{-1}$). The dispersion was drop-cast onto a mixed cellulose filter membrane, naturally dried at RT to obtain MXene films.

Fabrication of the superlattice EtDAB·4PbI_2 film

461 mg of PbI_2 and 100 mg of EtDAB were dissolved in 3 mL of DMF. The nylon membrane was then immersed in the resulting solution for 1 min. Subsequently, the substrate coated with EtDAB·4PbI_2 was removed and illuminated under incandescent light until the film color turned green. Finally, the film was

annealed at 100 °C for 30 min to obtain the EtDAB·4PbI_2 film.

Synthesis of $Co_3(HITP)_2$

A solution of cobalt(II) nitrate hexahydrate [$Co(NO_3)_2 \cdot 6H_2O$, 62.1 mmol·L^{-1}, 10 equiv.] in DMF (1.5 mL) was preheated at 65 °C. An aqueous solution of NaOAc (2 m, 2 mL) was added, followed by a solution of HATP·6HCl (5 mg, 0.0093 mmol, 1 equiv.) in water (1.5 mL). The resulting mixture was stirred at 750 rpm and heated in a 20 mL open glass vial at 65 °C for 2 h. The black powder was collected by filtration, washed with plenty of water and methanol, and dried under vacuum[29].

Characterization and measurements

The phase composition was analyzed using an X-ray diffractometer (D8 Discover Davinci, Germany). The surface morphology was characterized by field-emission scanning electron microscopy (FESEM; SU8220, Hitachi, Japan). The microstructure was examined using atomic force microscopy (AFM; NTEGRA, NT-MDT, Russia). The macroscopic surface morphology was scanned using a 3D laser scanning microscope (OLS5100, Olympus, Japan). Infrared thermal images were captured using a thermal imager (P20MAX V2, HIKMICRO, China). The digital multimeter was used to measure the sample conductivity. Pressure sensing properties of the samples were measured using a system comprising customized force gauges (M5-20 and M4-012, Mark-10, USA), a multichannel potentiostat/galvanostat (Autolab PGSTAT204, Metrohm, Switzerland) and data acquisition software. Temperature sensing properties of the samples were measured using a system comprising a heated stage, a multichannel potentiostat/galvanostat (Autolab PGSTAT204, Metrohm, Switzerland) and a thermometer (T2000-T6325 PRT, Xi'an Xiatech Electronics Co., Ltd., China; ST1004, Smart Sensor Holding Company Ltd., China). Gas sensing properties of the samples were measured using a source measure unit (Keithley 2611B, Tektronix, USA) and an LCR meter (Victor 4090B).

RESULTS AND DISCUSSION

Pressure module

High linearity, a proportional relationship between signal output and applied stimulus, is actively pursued in sensor design as it ensures straightforward measurement interpretation, reliable signal processing, and simplified calibration[32]. Conventional piezoresistive pressure sensors typically exhibit a distinct multi-stage non-linear response: at low pressures, rapid response originates from pronounced material deformation and formation of new conductive paths; as pressure increases, contact resistance stabilizes, and the response approaches saturation, resulting in reduced output signal variation. To overcome this limitation and achieve linearity across a broader pressure range, we introduce a structure–resistance dual-gradient pattern design fabricated via aerosol jet printing [Figure 2A]. Aerosol jet printing allows precise material deposition by ultrasonically atomizing liquid ink into aerosol droplets, which are then delivered by carrier gas to the print head, where they undergo aerodynamic focusing into a microscale jet[33]. Accordingly, a series of MXene/HEC inks with different mass ratios were prepared for aerosol jet printing.

To realize the dual-gradient pattern, stripes with precisely controlled heights and resistances were directly printed onto the MXene film [Supplementary Figures 5 and 6]. The stripe array exhibits a periodic height profile of "Low–Medium–High–Medium–Low", and the electrical resistance of the corresponding stripes follows the same spatial pattern [Supplementary Figure 7]. This design exploits sequential contact formation under applied pressure: the tallest stripes with the maximum resistance establish initial contact, creating conductive pathways with relatively low current increase. Subsequently, medium- and low-height stripes produce progressively faster changes in current. This spatially programmed contact sequence counteracts the inherent tendency toward saturation, smooths the transition across pressure regimes, and ultimately enhances linearity throughout the entire sensing range.

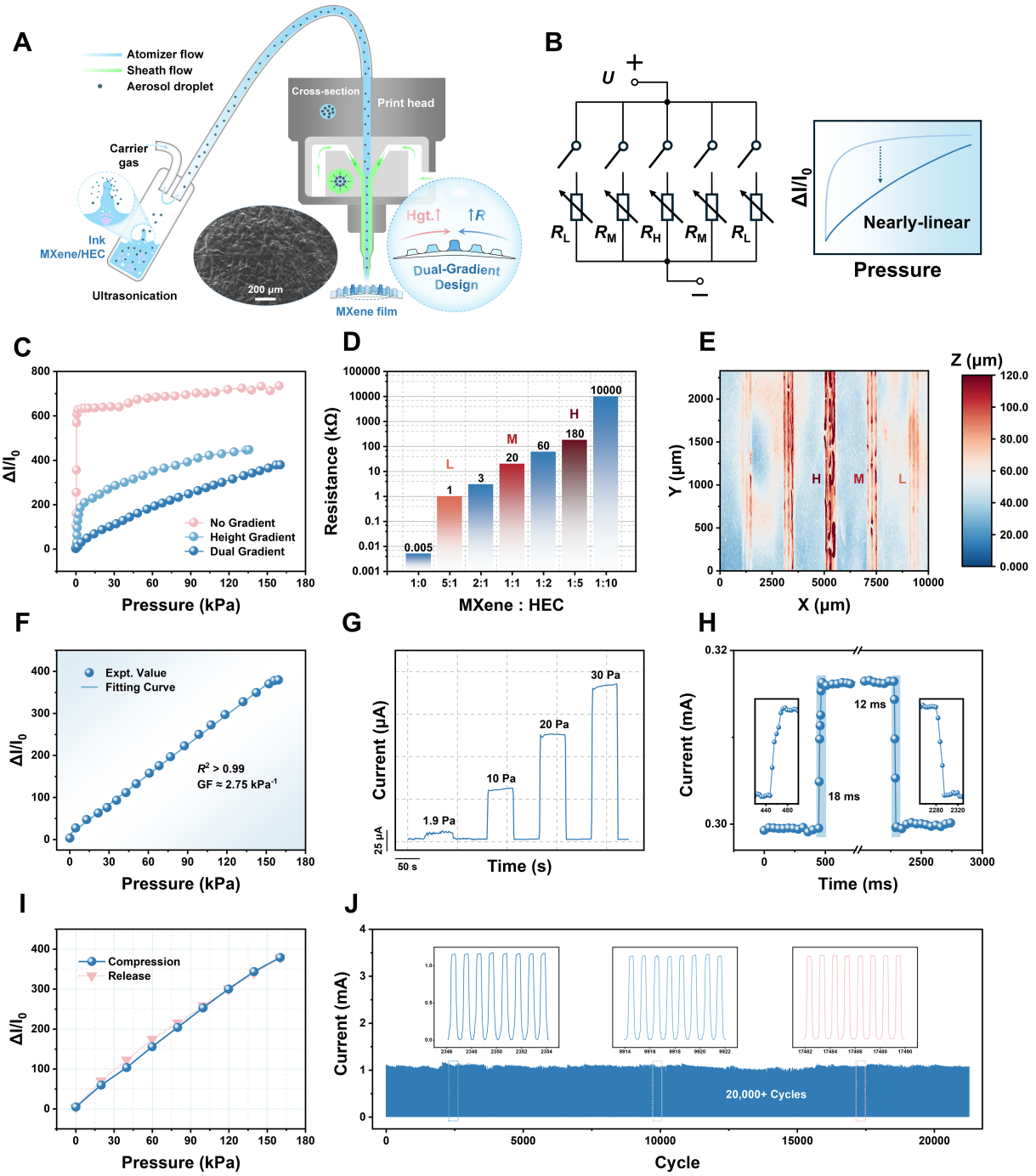

Figure 2. Pressure sensing performance enabled by the structure–resistance dual-gradient design. (A) Schematic illustration of the aerosol jet printing process used to fabricate dual-gradient stripes; (B) Equivalent electric circuit and schematics showing the strategy for achieving linearity; (C) Comparison of pressure responses with different gradient configurations; (D) Electrical characterization of printing inks with different MXene/HEC ratios; (E) The macroscopic surface morphology of the printed MXene film; (F) Pressure response of the dual-gradient patterned module with linear fitting; (G) Step response under low-pressure stimuli indicating the detection limit; (H) Dynamic response and recovery behavior of the pressure-sensing module; (I) Compression-release pressure response curves of the pressure module; (J) Stability test of the pressure module under more than 20,000 compression–release cycles. HEC: Hydroxyethyl cellulose; GF: gauge factor.

The sensing mechanism can be represented by the equivalent circuit shown in Figure 2B, where R_H, R_M, and R_L denote the resistance of the high, medium, and low stripes, respectively ($R_H > R_M > R_L$). Under applied pressure, these stripes establish contact sequentially, leading to a progressive increase in effective contact area

and a gradual reduction in contact resistance. The chronological connection of R_H, R_M, and R_L, together with their pressure-induced decrease in resistance, results in a continuous decline in equivalent circuit resistance. This staged contact process suppresses the rapid current increase at low pressure while enhancing conductive pathways at higher pressure, thereby mitigating early saturation and reducing marginal effects to yield a more linear pressure response.

Figure 2C illustrates the impact of gradient design on the response of the pressure module. With no gradients, unpatterned devices fabricated with pristine MXene films exhibited characteristic non-linear responses: $\Delta I/I_0$ increased rapidly at low pressures, quickly reached saturation, and settled in a stabilization plateau with negligible change. To address this limitation, we initially introduced a height gradient into the device, in which patterned stripes were printed using a single ink composition following the periodic height cycle described above. While this configuration improved linearity compared with unpatterned devices, the pressure-response curve still exhibited different gauge factors across the various sensing ranges with overall poor linearity [Supplementary Figure 8], consistent with previous reports employing analogous single-gradient strategies[34,35]. Hence, we engineered height–resistance dual-gradient stripes on the device to address this limitation. These results show that introducing height gradients alone is not enough to ensure linearity in the pressure–resistance behavior. We therefore engineered dual-gradient stripes with both height and resistance variations to overcome this limitation. To determine the resistance gradient, the electrical properties of MXene/HEC inks were evaluated by drop-casting onto filter membranes and measuring line resistance, providing guidance for optimizing printing parameters [Figure 2D]. Furthermore, we systematically investigated the influence of stripe width on the pressure response, as this geometric parameter critically affects the device linearity. Comparative studies of sensors with periodic stripe widths of 200, 300, and 500 μm revealed that wider printed stripes yield more linear responses, likely due to improved pressure distribution and more uniform contact formation [Supplementary Figure 9]. The measured surface morphology of the printed film confirms the periodic gradient structure, with stripe heights of approximately 120, 100, and 70 μm, respectively [Figure 2E].

The optimized sensor exhibits linear pressure sensing with a sensitivity of 2.75 kPa^{-1} across a pressure range up to 160 kPa. The sensor exhibits high linearity ($R^2 > 0.99$) across a broad sensing range, attributable to the dual-gradient design [Figure 2F]. Step tests conducted within the low-pressure range demonstrate a detection limit of 1.9 Pa [Figure 2G], while the sensor exhibits rapid response and recovery times of 18 and 12 ms, respectively, enabling real-time tracking of dynamic human physiological signals [Figure 2H]. Frequency response testing reveals excellent dynamic stability, with consistent output amplitude maintained over a broad frequency range from 0.5 to 4 Hz [Supplementary Figure 10]. Step pressure tests confirm stable and repeatable responses across a wide pressure range [Supplementary Figure 11]. Slight deviation between compression and release sensing curves indicates excellent reversibility and negligible hysteresis [Figure 2I]. After more than 20,000 compression-release cycles, no significant degradation in response was observed, demonstrating excellent mechanical durability for long-term applications [Figure 2J]. Owing to the elastic substrate having a much lower Young's modulus than the sensing materials, the sensor exhibits exceptional strain insensitivity, with negligible resistance variation (< 0.5%) under applied strains up to 40% [Supplementary Figure 12], improving robustness against routine stretching deformations. To evaluate its flexibility, the pressure module was bent from 0° to 120°, indicating that the pressure module maintains stable electrical behavior under bending deformation [Supplementary Figure 13].

Temperature module

The temperature module operates via junction potential formation at the MXene/EtDAB·4PbI_2 junction, where temperature variation induces a change in the potential difference (ΔV), generating a measurable open-circuit voltage (V_{oc}) for temperature detection [Figure 3A]. The flexible sensor thus enables direct and

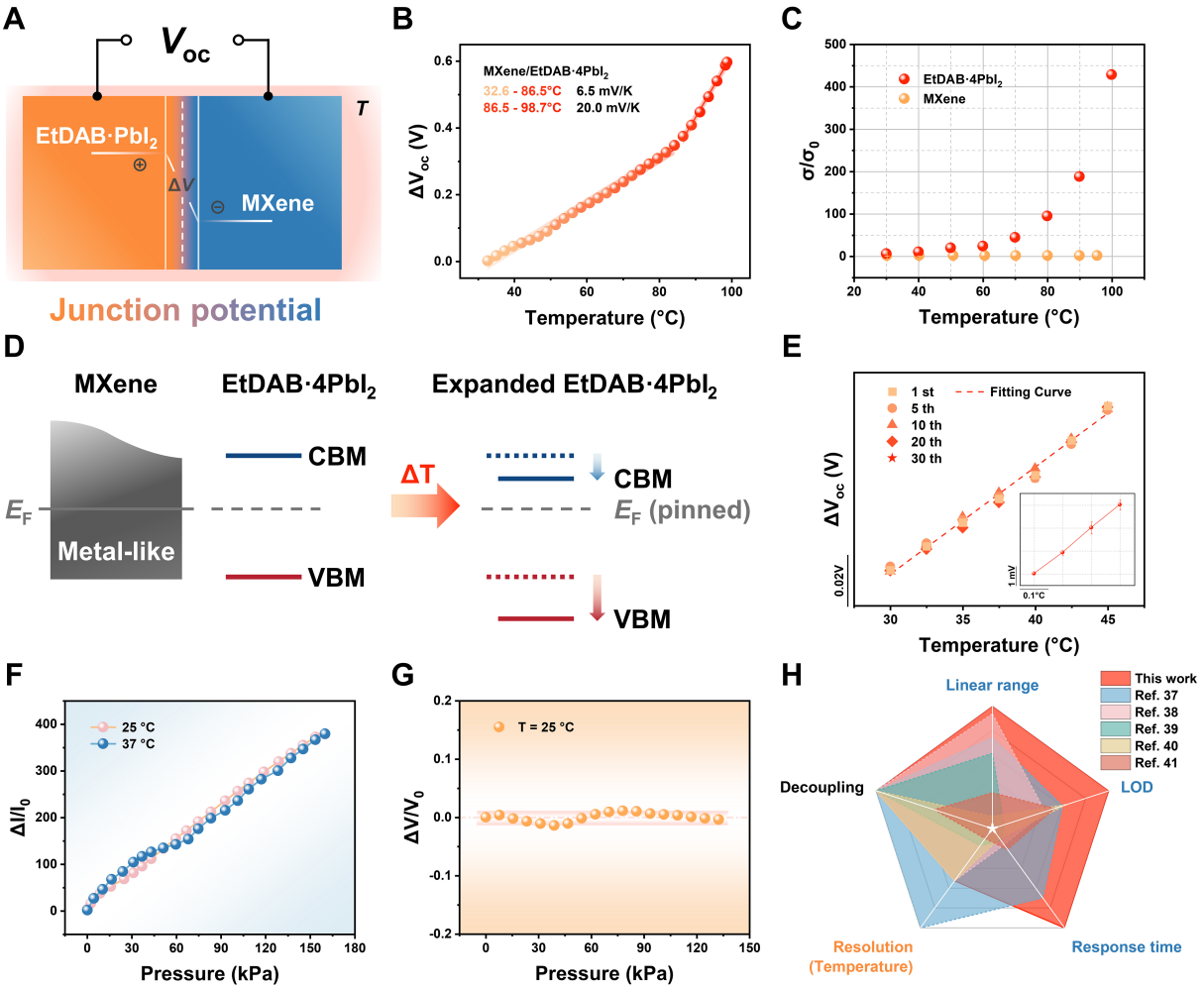

Figure 3. Junction potential–based temperature sensing of the MXene/EtDAB·4PbI$_2$ junction and its intrinsic signal decoupling performance. (A) Schematic illustration of the junction potential–based mechanism; (B) Temperature-dependent open-circuit voltage change (ΔV_{oc}); (C) Normalized electrical conductivity of MXene and EtDAB·4PbI$_2$ *vs.* temperature; (D) Schematic illustration of the temperature-induced band modulation mechanism at the MXene/EtDAB·4PbI$_2$ junction; (E) Repeatability of the temperature module during thirty heating–cooling cycles, with high-resolution temperature response to minute temperature variations (inset); (F) Pressure response measured at different ambient temperatures; (G) Temperature response under external mechanical loading; (H) Radar plot comparing key performance metrics of this work with reported pressure–temperature sensors. The error bars represent the standard deviation based on a sample size of three (n = 3). CBM: Conduction band minimum; VBM: valence band maximum; LOD: limit of detection.

instant temperature monitoring via voltage readout. The temperature sensing sensitivity is defined as $S = d(\Delta V_{oc})/dT$, where ΔV_{oc} represents the open-circuit voltage change between MXene and EtDAB·4PbI$_2$ films, and dT represents the corresponding temperature variation. Figure 3B exhibits a sensitivity of 6.5 mV/K over the temperature range from 32.6 to 86.5 °C, which increases to 20.0 mV/K at temperatures above 86.5 °C. To elucidate the sensing mechanism, we investigated the temperature-dependent electrical conductivity of both materials. The electrical conductivity of MXene remains practically unchanged with the increase in temperature, which is expected from its metallic nature [Figure 3C]. In contrast, EtDAB·4PbI$_2$ showed a clear temperature-dependent behavior indicating that it plays a leading role in the temperature sensing performance of the assembled temperature module [Figure 3C]. Furthermore, the current–voltage characteristics of the material pair confirm the formation of a Schottky-like junction [Supplementary Figure 14].

Figure 3D schematically illustrates the temperature-induced energy band modulation mechanism at the MXene/EtDAB·4PbI_2 junction. Temperature variations induce lattice thermal expansion, which shifts the band edges of EtDAB·4PbI_2. Due to the metal-like electronic nature and high density of states of MXene, the interfacial Fermi level is effectively pinned and remains largely insensitive to thermal fluctuations. In contrast, the conduction and valence band edges of EtDAB·4PbI_2 respond asymmetrically to temperature variations, leading to band offsets relative to the pinned Fermi level. This behavior can be described by a linear thermal expansion model based on deformation potentials estimated from density functional theory (DFT) calculations [Supplementary Note 1 and Supplementary Figure 15][36]. These asymmetric band-edge shifts induce a redistribution of charge carriers and generate a thermally driven potential difference across the Schottky-like junction. Compared with pristine PbI_2, the intercalation of EtDAB enhances lattice compliance and electronic asymmetry, amplifying the valence-band-dominated response under temperature variation. Consequently, temperature sensing in the device is mainly attributed to band modulation of EtDAB·4PbI_2 mediated by interfacial charge redistribution rather than classical thermoelectric effects or Schottky barrier height modulation.

Over thirty heating and cooling cycles confirmed negligible hysteresis and excellent sensing repeatability and stability of the sensor [Figure 3E and Supplementary Figure 16]. As shown in Figure 3E, the sensor exhibits a high temperature resolution, capable of distinguishing temperature differences as small as 0.1 K, with a rapid response and recovery time of 1.0 and 2.8 s respectively [Supplementary Figure 17]. To verify the effective decoupling of the pressure and temperature sensing mechanisms, cross-sensitivity tests were systematically conducted. The pressure module maintains accurate sensing regardless of ambient temperature variations, with response curves at 25 and 37 °C exhibiting nearly perfect overlap, thereby confirming its insensitivity to temperature fluctuations [Figure 3F]. Similarly, the temperature response was verified to be pressure-insensitive. Under a constant ambient temperature of 25 °C, the temperature module exhibited ignorable variation when subjected to external mechanical loading [Figure 3G]. In addition, the temperature module demonstrates remarkable strain-suppression capability due to the same modulus engineering strategy. At RT, the response signal of the temperature module remains highly stable (variation < 2%) even under tensile strain up to 40% [Supplementary Figure 18]. The temperature module also maintained a nearly unchanged voltage output at 25 °C under bending angles from 0° to 120° [Supplementary Figure 19]. Furthermore, a comparison with recently reported pressure–temperature sensors demonstrates the superior overall performance of our device [Figure 3H, Supplementary Table 1 and Supplementary Note 2][37-41].

Gas module

Figure 4A schematically illustrates the experimental configuration for gas sensing measurements[12]. Target gas and carrier gas streams were precisely regulated by mass flow controllers and mixed in a temperature-controlled mixing vessel to ensure a stable and homogeneous gas composition before entering the sealed test chamber. The sensor was electrically connected to an LCR meter for real-time resistance monitoring, with data continuously recorded and processed via computer interface. This configuration enables accurate control of gas concentration and reliable monitoring of the sensor response under varying gas-exposure conditions.

Figure 4B schematically illustrates the sensing mechanism of the gas-sensing module. Upon exposure to NO molecules, the $Co_3(HITP)_2$ framework exhibits strong adsorption at the open Co sites, which induces charge redistribution within the MOF layer[42,43]. Density-driven electron transfer occurs from the EEG to the adsorbed NO-MOF complex, leading to a partial depletion of holes in the *p*-type EEG. As a result, the Fermi level of the hybrid system shifts upward toward the Dirac point, effectively reducing the *p*-type character of EEG. This hole depletion weakens the dominant hole conduction in EEG, giving rise to a decrease in conductivity and a corresponding increase in resistance[44,45]. Therefore, the gas sensing response originates

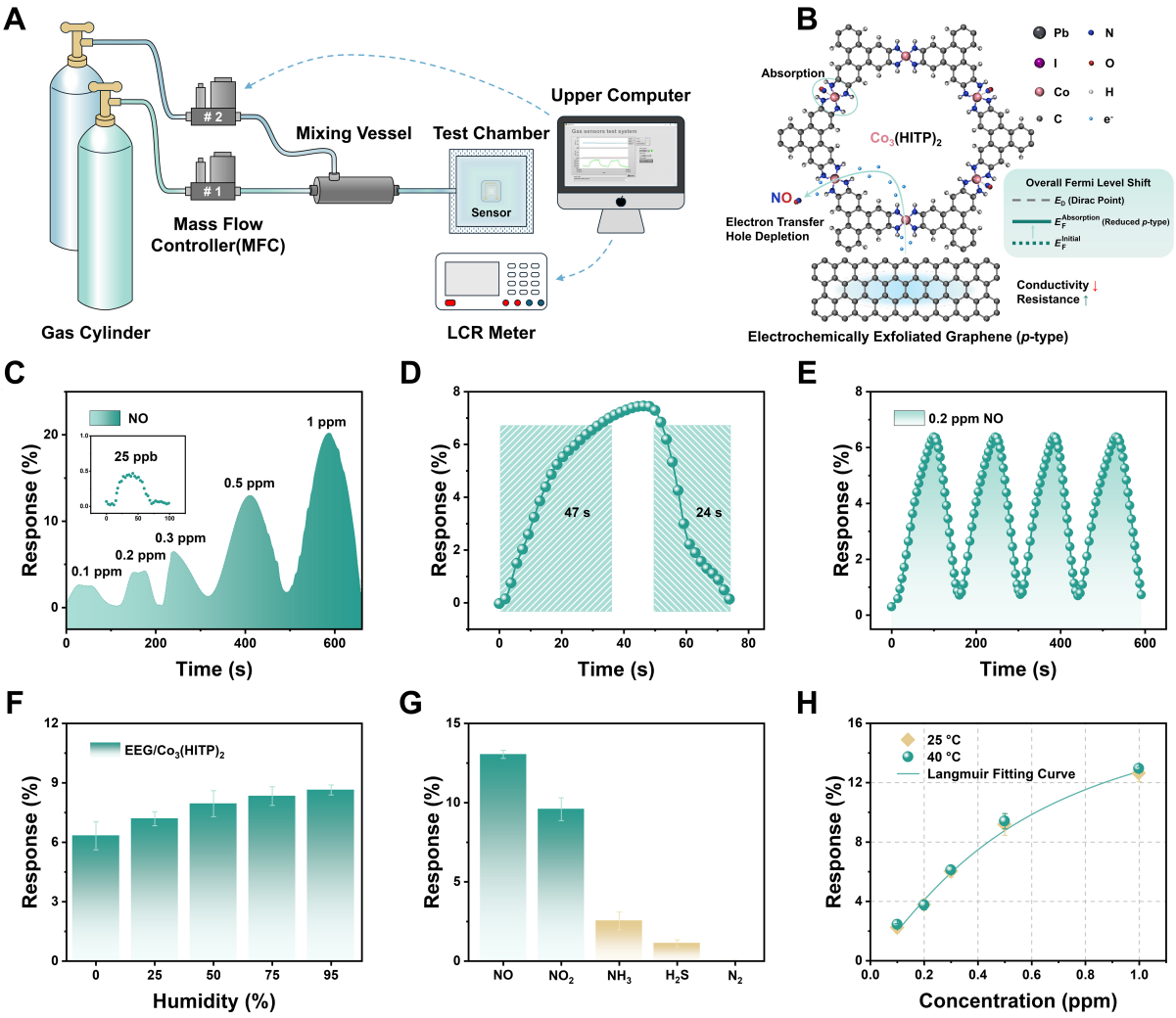

Figure 4. NO gas sensing performance and sensing mechanism of the EEG/Co_3(HITP)$_2$ hybrid. (A) Schematic illustration of the experimental equipment for gas sensing measurements; (B) Schematic illustration of the NO sensing mechanism based on adsorption-induced charge transfer at the EEG/Co_3(HITP)$_2$ interface; (C) Dynamic responses of the gas-sensing module to NO at the detection limit of 25 ppb and at stepwise concentrations from 0.1 to 1 ppm; (D) Response and recovery characteristics of the sensor upon exposure to NO; (E) Repeatability of the sensor response under periodic NO injection; (F) Gas sensing response of the sensor under different humidity conditions; (G) Selectivity of the gas module toward NO compared with other gases; (H) Gas sensing responses measured at different ambient temperatures. The error bars represent the standard deviation based on a sample size of three (n = 3). NO: Nitric oxide; EEG: electrochemically exfoliated graphene.

from adsorption-induced charge transfer at the MOF/EEG interface and the associated modulation of the overall Fermi level of the hybrid system, which is a different mechanism from the current- and voltage-based readouts of pressure and temperature modules, respectively.

The gas module exhibited a clear response to NO at the detection limit of 25 ppb, confirming its capability for trace NO detection. In addition, stepwise NO exposure from 0.1 to 1 ppm under ambient conditions demonstrated a clear dose-dependent response throughout the tested concentration range [Figure 4C]. When exposed to 1 ppm NO, the device exhibited response and recovery times of approximately 47 and 24 s, respectively [Figure 4D]. Results in Figure 4E show that periodic introduction of 0.2 ppm NO gives excellent repeatability, with stable response amplitude maintained over multiple test cycles.

Moisture is a key interference factor for gas sensors, particularly in respiratory analysis where EB contains a significant amount of water vapor. We systematically tested the device's response under varying humidity conditions [Figure 4F, Supplementary Figures 20 and 21]. The device response was normalized to obtain relative variation curves given by $Re(X\%)/Re(0\%)$, where $X\%$ represents the relative humidity. We found that the $Co_3(HITP)_2$-based sensor effectively reduces humidity interference, which we attribute to hydrophobic benzene rings in the $Co_3(HITP)_2$ structure that inhibit water adsorption. Long-term stability studies show that the device has robust environmental stability in air for 14 days, while 0.5 ppm of NO was introduced each day for testing and subsequent monitoring [Supplementary Figure 22].

The ability to accurately identify and distinguish target gases within complex mixtures is critical for medical diagnostic applications. The sensor showed preferential sensitivity to NO and NO_2, with higher responses than to other common gases, including ammonia (NH_3), hydrogen sulfide (H_2S), and nitrogen (N_2) [Figure 4G]. To evaluate cross-sensitivity between temperature and gas sensing, experiments were conducted at 25 and 40 °C [Figure 4H]. The gas response remained consistent across the testing range, indicating temperature-independent NO detection near physiological temperatures, a critical requirement for EB analysis. This temperature insensitivity, combined with a chemiresistive readout mechanism orthogonal to both the piezoresistive current and the open-circuit voltage, further confirms the intrinsic three-way signal decoupling in the integrated multimodal sensor.

Wearable application

To validate practical clinical applications, we integrated the sensor into a conventional N95 mask, creating a smart respiratory monitoring system. This integrated sensing mask enables simultaneous detection of multiple respiratory parameters, including RR, breathing depth, EB temperature, and NO concentration, enabling comprehensive respiratory health assessment in a comfortable, minimally invasive format [Figure 5A]. Specifically, the pressure, temperature, and NO-sensing modules provide complementary mechanical, thermal, and chemical information for respiratory assessment. The pressure module reflects airflow-induced pressure fluctuations for extracting RR, breathing depth, and abnormal breathing events; the temperature module records exhaled-breath temperature variations for identifying breathing modes; and the gas-sensing module detects exhaled NO as an inflammatory gas biomarker.

The pressure-sensing module allows distinguishing diverse breathing states through the analysis of airflow-induced pressure variations inside the mask. The sensing signals in Figure 5B and C show a series of distinct peak patterns corresponding to different breathing depths (shallow, normal, and deep) and breathing rates (slow, normal, and quick), as well as abnormal breathing events, such as coughing. These distinct patterns prove that the sensor can meet the requirements for monitoring both normal respiratory activity and common pathological breathing behaviors in real-world scenarios.

Most respiratory monitoring masks are equipped with monofunctional sensors limited to single-parameter detection. Such single-modal strategies are susceptible to interference under complex breathing conditions, making it challenging to reliably distinguish between nasal breathing and mouth breathing. For example, when breath pressure intensity and frequency are comparable, pressure signals alone are often insufficient to differentiate deep nasal breathing from mouth breathing. Respiratory monitoring devices capable of accurately identifying nasal *vs.* mouth breathing can provide early warnings of breathing difficulties, particularly among patients with asthma and children[46]. Consequently, accurate nasal and mouth breathing differentiation possesses considerable potential for practical respiratory health monitoring. Our multimodal sensor addresses this limitation by integrating temperature sensing. When subjects breathed through the nose or mouth, distinct temperature variations occurred inside the mask, enabling accurate differentiation of breathing states. Nasal breathing produced relatively small voltage amplitude variations, in contrast to mouth

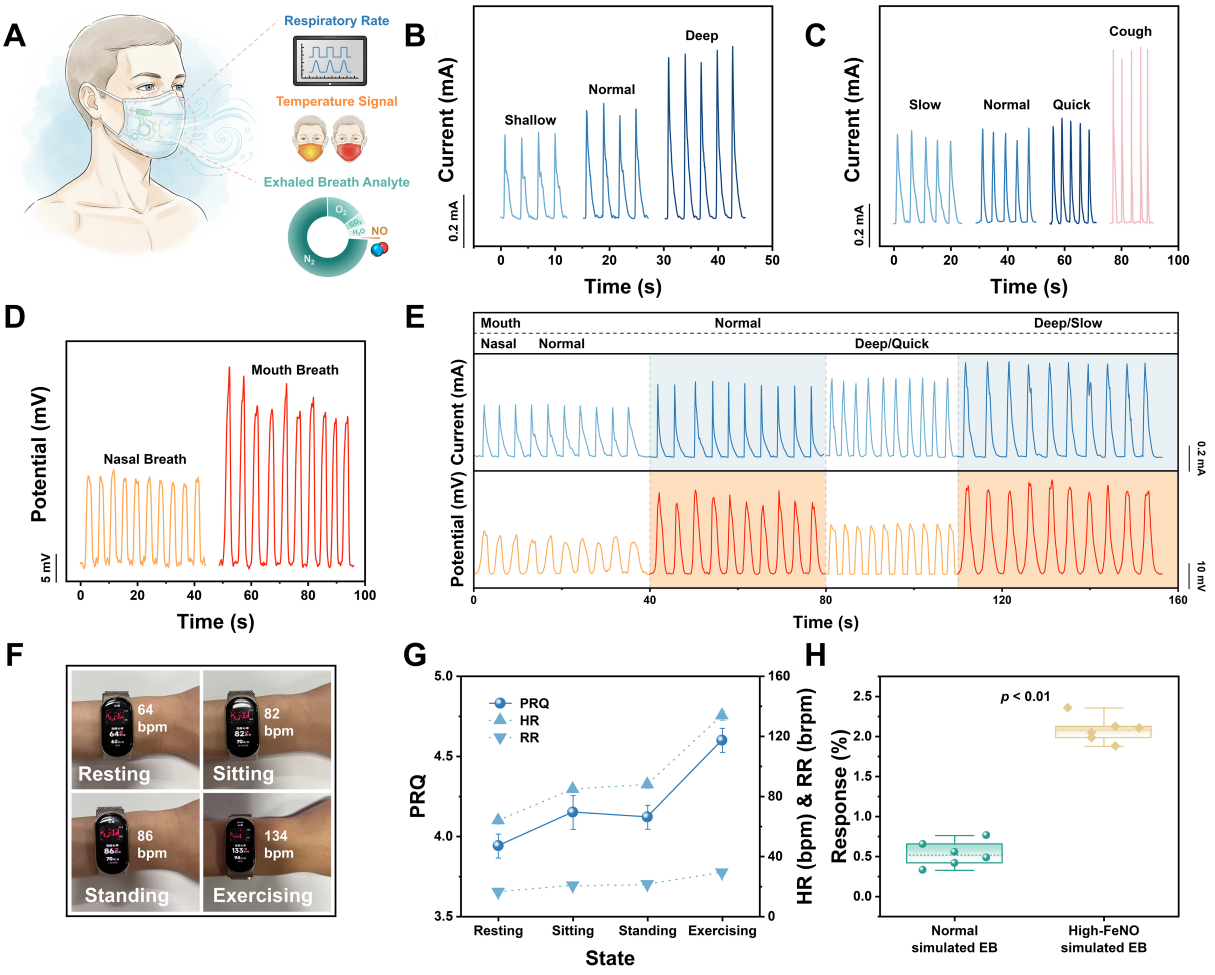

Figure 5. Wearable respiratory monitoring enabled by the integrated multimodal sensing mask. (A) Schematic illustration of the sensor integrated into a wearable mask for respiratory monitoring; (B) Pressure sensing signals corresponding to different breathing depths; (C) Pressure sensing signals corresponding to different breathing rates; (D) Temperature sensing responses distinguishing nasal and mouth breathing; (E) Multimodal identification of diverse breathing behaviors based on combined pressure and temperature signals; (F) HR monitoring under different activity states; (G) PRQ calculated from HR and RR under various physiological conditions. The error bars represent the standard deviation based on a sample size of three (n = 3); (H) Differentiation of exhaled NO levels between normal simulated EB and high-FeNO simulated EB. Box plots were generated from six repeated measurements for each condition (n = 6). The P-value was determined by paired t-test (two-tailed). Human-related mask tests were conducted by the first author as self-experiments, and no external volunteers or patients were recruited. HR: Heart rate; PRQ: pulse respiration quotient; RR: respiratory rate; NO: nitric oxide; EB: exhaled breath; FeNO: fractional exhaled nitric oxide.

breathing, which led to a markedly larger change in signal amplitude [Figure 5D]. Infrared thermal imaging confirmed these findings, showing higher temperature variations inside the mask during mouth breathing than during nasal breathing [Supplementary Figure 23]. The smart mask successfully identified multiple breathing patterns, including normal nasal breath, normal mouth breathing, deep and rapid nasal breathing, and deep and slow mouth breathing [Figure 5E], demonstrating that multimodal sensing substantially improves detection accuracy and broadens the range of practical application scenarios.

RR, together with heart rate (HR), is widely recognized as a significant indicator of clinical acuity[47]. Even deviations of only 4 breaths per minute (brpm) from normal range can indicate severe clinical deterioration, highlighting the critical need for precise respiratory monitoring[48]. Variations in posture and physical activity modulate both HR and RR, making their continuous and accurate monitoring essential in wearable health

systems. Our smart mask resolved distinct changes in HR and RR across different activity states, including resting, sitting, standing, and exercising [Figure 5F and Supplementary Figure 24]. During rest, both HR and RR remained at relatively low levels, with average values of approximately 63.8 beats per minute (bpm) and 16.2 brpm, respectively. When changing to sitting and standing postures, HR and RR increased to 84.7 bpm/20.4 brpm and 87.8 bpm/21.3 brpm, respectively. This increase in RR is mainly due to posture-related variation in blood distribution[49]. During exercise, increased muscular activity substantially raised ventilatory demand, resulting in a markedly higher RR of 29.1 brpm and a HR of 133.8 bpm. Based on these measurements, we calculated the pulse respiration quotient (PRQ), defined as the ratio of heart rate to respiratory rate (PRQ = HR/RR), a composite metric characterizing cardiopulmonary function[50,51]. PRQ values were 3.94, 4.15, 4.12, and 4.60 under the four aforementioned conditions, respectively, indicating variation with activity levels [Figure 5G]. Generally, HR is approximately four times higher than RR (PRQ ≈ 4)[52]. In patients with asthma and COPD, chronic airflow limitation and increased respiratory load are associated with elevations in both HR and RR[53], resulting in a persistently reduced PRQ compared with healthy individuals. In contrast, asthma is characterized by episodic bronchoconstriction, during which temporal increases in respiratory effort and breathing frequency may lead to deviations in HR, RR, and PRQ from baseline levels[54,55]. It should be noted that PRQ was calculated from stable breathing segments under controlled testing conditions, while obvious non-breathing actions such as speaking and swallowing were avoided during data acquisition. Artifact-detection and filtering algorithms are expected to improve RR extraction under complex daily activities.

Clinical practice has established that FeNO levels below 25 ppb in adults indicate a low likelihood of eosinophilic airway inflammation, whereas levels above 50 ppb suggest high probability of significant eosinophilic inflammation[56]. These cut points are widely used in asthma assessment and management, as elevated FeNO correlates with eosinophilic airway inflammation in asthma patients[57,58]. In patients with COPD and asthma-chronic obstructive pulmonary disease overlap (ACO), FeNO levels correlate with disease status and severity, providing valuable non-invasive biomarker information for identifying airway inflammation[59,60]. In controlled mask-based testing, the mask showed significant response differences between normal simulated EB and high-FeNO simulated EB with controlled NO supplementation, demonstrating its capability to distinguish low-concentration NO-level changes in simulated EB [Supplementary Figure 25]. Boxplot analysis indicates that the mask effectively distinguishes normal simulated EB from high-FeNO simulated EB, with an approximately 1.5% difference in response ($P < 0.01$) [Figure 5H]. This sensing resolution falls within the clinically relevant FeNO range, suggesting potential applicability for monitoring inflammatory airway diseases such as asthma and COPD.

CONCLUSION

We developed a flexible, compact, multimodal respiratory sensor with intrinsic device-level signal decoupling. Our sensor integrates vertically stacked pressure, temperature, and NO gas-sensing modules that operate via orthogonal transduction mechanisms (piezoresistive current, junction potential, and chemiresistive response). This configuration achieves simultaneous multimodal detection without algorithm-based signal separation. The compact vertically stacked architecture, together with independent readout channels and distinct transduction mechanisms, enables different respiratory stimuli to be converted into distinguishable electrical outputs, thereby reducing signal interference while maintaining a small device footprint suitable for wearable applications. The successful integration of the sensor into a wearable mask demonstrates its ability to monitor key respiratory indicators, showing its potential for continuous, wearable respiratory health monitoring for the management of airway inflammatory diseases.

Nevertheless, the current wearable validation remains a proof-of-concept demonstration based on limited testing and simulated high-FeNO conditions. Further studies involving a larger number of participants, long-term monitoring under real breathing environments, and comparison with clinically approved FeNO

analyzers are needed to validate its practical diagnostic reliability. Future work will also focus on integrating the sensor with miniaturized readout systems for more practical wearable respiratory healthcare applications.

DECLARATIONS

Acknowledgments

We gratefully acknowledge Hao Ouyang (ORCID: 0009-0009-1728-6264) and all fellow students for their wholehearted encouragement before sunrise.

Authors' contributions

Conceptualization: Wang, R.
Data curation: Song, Z.; Shi, L.
Formal analysis: Song, Z.
Funding acquisition: Cheng, Y.; Sun, J.; Wang, R.
Investigation: Song, Z.
Methodology: Wang, R.
Project administration: Cheng, Y.; Sun, J.; Wang, R.
Resources: Shi, L.; Cheng, Y.; Wang, G. E.; Wang, R.
Supervision: Huang, C.; Sheremet, E.; Rodriguez, R. D.; Shi, L.; Cheng, Y.; Sun, J.; Wang, G. E.
Validation: Song, Z.; Huang, C.; Shi, L.; Wang, G. E.
Visualization: Song, Z.
Writing - original draft: Song, Z.
Writing - review and editing: Huang, C.; Sheremet, E.; Rodriguez, R. D.; Wang, R.

Availability of data and materials

All data needed to evaluate the conclusions are available in the manuscript and the Supplementary Materials.

AI and AI-assisted tools statement

During the preparation of this manuscript, the AI tools Gemini 2.5 Flash (Google, released 2025-06-17) and Seedream 3.0 (ByteDance, released 2025-04-16) were used solely for improving schematic illustrations. The AI tool GPT-5.2 (OpenAI, released 2025-12-11) was used solely for language editing. These tools did not influence the study design, data collection, data analysis, interpretation, or the scientific content of the work. All authors take full responsibility for the accuracy, integrity, and final content of the manuscript.

Financial support and sponsorship

This work was supported by the National Key Research and Development Program of China (Grant No. 2024YFB3814100), National Natural Science Foundation of China [62471459, U24A20228, 62261136551 (Russian Science Foundation grant No 23-42-00081) and 62301540], the Chinese Academy of Sciences Project for Young Scientists in Basic Research (Grant No.YSBR-109), Joint Project "ActFiber-FFG/CAS: 931688/030GJHZ2025029MI" managed by Austrian Research Promotion Agency (FFG) and Chinese Academy of Sciences (CAS), Shanghai International Science and Technology Cooperation Project (23520711000) from Science and Technology Commission of Shanghai Municipality.

Conflicts of interest

All authors declared that there are no conflicts of interest.

Ethical approval and consent to participate

This study involved only noninvasive, low-risk physiological monitoring conducted by the first author as self-experiments under routine breathing conditions and controlled simulated exhaled-breath conditions, without any invasive procedures or risks to human health. According to Article 32 of the Measures for the Ethical Review of Life Science and Medical Research Involving Human Subjects (Trial), this study meets the criteria for exemption from ethical review. The participant provided informed consent prior to participation in the experiment.

Consent for publication

Not applicable.

Supplementary Materials

Supplementary Materials

REFERENCES

1. Oh, J.; Kim, S.; Yim, Y.; et al.; GBD 2023 Global Chronic Respiratory Disease and Covid Collaborators. Global, regional, and national burden of chronic respiratory diseases and impact of the COVID-19 pandemic, 1990-2023: a Global Burden of Disease study. *Nat. Med.* **2026**, *32*, 197-223. DOI PubMed
2. GBD 2019 Chronic Respiratory Diseases Collaborators. Global burden of chronic respiratory diseases and risk factors, 1990-2019: an update from the Global Burden of Disease Study 2019. *EClinicalMedicine* **2023**, *59*, 101936. DOI PubMed PMC
3. Cao, Z.; Tong, X.; He, L.; et al. Burden of chronic obstructive pulmonary disease and its attributable risk factors in 204 countries and territories, 1990-2021: results from the Global Burden of Disease Study 2021. *BMJ. Public. Health.* **2026**, *4*, e002489. DOI PubMed PMC
4. Alves Pegoraro, J.; Guerder, A.; Similowski, T.; Salamitou, P.; Gonzalez-Bermejo, J.; Birmelé, E. Detection of COPD exacerbations with continuous monitoring of breathing rate and inspiratory amplitude under oxygen therapy. *BMC. Med. Inform. Decis. Mak.* **2025**, *25*, 101. DOI PubMed PMC
5. Yentes, J. M.; Fallahtafti, F.; Denton, W.; Rennard, S. I. COPD patients have a restricted breathing pattern that persists with increased metabolic demands. *COPD* **2020**, *17*, 245-52. DOI PubMed PMC
6. Zulkifli, N. A.; Jeong, W.; Kim, M.; et al. 3D-printed magnetic-based air pressure sensor for continuous respiration monitoring and breathing rehabilitation. *Soft. Sci.* **2024**, *4*, 20. DOI
7. Xu, M.; Liu, F.; Chen, L.; et al. Zwitterionic poly(ionic liquid) hydrogel electrolytes with high-speed ion conduction channels for dendrite-free, long-enduring zinc-ion batteries and flexible electronics. *Energy. Storage. Mater.* **2025**, *80*, 104373. DOI
8. Tipton, M. J.; Harper, A.; Paton, J. F. R.; Costello, J. T. The human ventilatory response to stress: rate or depth? *J. Physiol.* **2017**, *595*, 5729-52. DOI PubMed PMC
9. Paredi, P.; Kharitonov, S. A.; Barnes, P. J. Correlation of exhaled breath temperature with bronchial blood flow in asthma. *Respir. Res.* **2005**, *6*, 15. DOI PubMed PMC
10. Annesi-Maesano, I.; Dinh-Xuan, A. T. Is exhaled nitric oxide a marker of air pollution effect? *Eur. Respir. J.* **2016**, *47*, 1304-6. DOI PubMed
11. Heng, W.; Yin, S.; Chen, Y.; Gao, W. Exhaled breath analysis: from laboratory test to wearable sensing. *IEEE. Rev. Biomed. Eng.* **2025**, *18*, 50-73. DOI PubMed PMC
12. Pan, J.; Li, Y.; Tian, T.; Tang, Z.; Lian, Z.; Ma, N. Highly sensitive humidity sensor based on NaCl-$BiFeO_3$ for noncontact sensing. *ACS. Appl. Electron. Mater.* **2025**, *7*, 1842-51. DOI
13. Al-Halhouli, A.; Albagdady, A.; Rabadi, A.; Hamdan, M.; Abu-Khalaf, J.; Abu-Abeeleh, M. Screen-printed wearable sensors for continuous respiratory rate monitoring: fabrication, clinical evaluation, and point-of-care potential. *Mater. Adv.* **2024**, *5*, 9586-95. DOI
14. Dong, H.; Li, X.; Liu, Y.; et al. Wearable, breathable, and wireless gas sensor enables highly selective exhaled ammonia detection and real-time noninvasive illness diagnosis. *ACS. Sens.* **2025**, *10*, 3964-75. DOI
15. Shin, J.; Jeong, B.; Kim, J.; et al. Sensitive wearable temperature sensor with seamless monolithic integration. *Adv. Mater.* **2020**, *32*, e1905527. DOI PubMed
16. Ye, L.; Wu, F.; Xu, R.; et al. Face mask integrated with flexible and wearable manganite oxide respiration sensor. *Nano. Energy.* **2023**, *112*, 108460. DOI
17. Li, Y.; Wang, R.; Wang, G. E.; et al. Mutually noninterfering flexible pressure-temperature dual-modal sensors based on conductive metal-organic framework for electronic skin. *ACS. Nano.* **2022**, *16*, 473-84. DOI PubMed
18. Shi, W.; Yang, X.; Lei, L.; et al. Human respiration monitoring using humidity and temperature dual-modal sensors for temperature-insensitive humidity sensing and synchronous temperature sensing. *Sens. Actuators. A. Phys.* **2025**, *395*, 117008. DOI
19. Ma, B.; Huang, K.; Chen, G.; et al. A dual-mode wearable sensor with coupled ion and pressure sensing. *Soft. Sci.* **2024**, *4*, 8. DOI
20. Kim, D. H.; Lu, N.; Ma, R.; et al. Epidermal electronics. *Science* **2011**, *333*, 838-43. DOI PubMed
21. Hua, Q.; Sun, J.; Liu, H.; et al. Skin-inspired highly stretchable and conformable matrix networks for multifunctional sensing. *Nat. Commun.* **2018**, *9*, 244. DOI PubMed PMC

22. Jia, Q.; Ye, W.; Zhang, C.; et al. Wearable multimodal sensing system for synchronously health-environmental monitoring via hybrid neuroevolutionary signal decoupling. *Nano. Lett.* **2025**, *25*, 9726-33. DOI PubMed
23. Fang, Y.; Ouyang, H.; Cheng, Y.; et al. Ultrasensitive multi-degree-of-freedom piezoionic sensor via synergistic hydrogel-ion interactions. *Nat. Commun.* **2025**, *17*, 893. DOI PubMed PMC
24. Wu, T.; Li, Y. T.; Zhao, L.; et al. Recent progress on flexible multimodal sensors: decoupling strategies, fabrication and applications. *Adv. Mater.* **2026**, *38*, e21375. DOI PubMed PMC
25. Zhou, Z.; Wu, H.; Fu, J.; et al. Fully integrated passive wireless sensor with mechanical-electrical double-gradient for multifunctional healthcare monitoring. *Nano. Lett.* **2024**, *24*, 14781-9. DOI PubMed
26. Zhou, Z.; Jin, Y.; Fu, J.; et al. Smart wireless flexible sensing system for unconstrained monitoring of ballistocardiogram and respiration. *npj. Flex. Electron.* **2025**, *9*, 388. DOI
27. Mariello, M.; Rosenthal, J. D.; Cecchetti, F.; et al. Wireless, battery-free, and real-time monitoring of water permeation across thin-film encapsulation. *Nat. Commun.* **2024**, *15*, 7443. DOI PubMed PMC
28. Wang, G. E.; Xu, G.; Zhang, N. N.; Yao, M. S.; Wang, M. S.; Guo, G. C. From lead iodide to a radical form lead-iodide superlattice: high conductance gain and broader band for photoconductive response. *Angew. Chem. Int. Ed. Engl.* **2019**, *58*, 2692-5. DOI PubMed
29. Chen, T.; Dou, J. H.; Yang, L.; et al. Continuous electrical conductivity variation in M_3(Hexaiminotriphenylene)$_2$ (M = Co, Ni, Cu) MOF alloys. *J. Am. Chem. Soc.* **2020**, *142*, 12367-73. DOI PubMed
30. Kirchgessner, M.; Sreenath, K.; Gopidas, K. R. Understanding reactivity patterns of the dialkylaniline radical cation. *J. Org. Chem.* **2006**, *71*, 9849-52. DOI PubMed
31. Zhang, P.; He, P.; Zhao, Y.; et al. Oxidating fresh porous graphene networks toward ultra-large graphene oxide with electrical conductivity. *Adv. Funct. Mater.* **2022**, *32*, 2202697. DOI
32. Pyo, S.; Lee, J.; Bae, K.; Sim, S.; Kim, J. Recent progress in flexible tactile sensors for human-interactive systems: from sensors to advanced applications. *Adv. Mater.* **2021**, *33*, e2005902. DOI PubMed
33. Xu, B.; Yang, M.; Cheng, W.; et al. Precision aerosol-jet micropatterning of liquid metal for high-performance flexible strain sensors. *Nat. Commun.* **2025**, *16*, 7920. DOI PubMed PMC
34. Geng, D.; Chen, S.; Chen, R.; et al. Tunable wide range and high sensitivity flexible pressure sensors with ordered multilevel microstructures. *Adv. Mater. Technol.* **2022**, *7*, 2101031. DOI
35. Wang, S.; Deng, W.; Yang, T.; et al. Bioinspired MXene-based piezoresistive sensor with two-stage enhancement for motion capture. *Adv. Funct. Mater.* **2023**, *33*, 2214503. DOI
36. Wang, Y.; Zhang, Y.; Zhang, P.; Zhang, W. High intrinsic carrier mobility and photon absorption in the perovskite $CH_3NH_3PbI_3$. *Phys. Chem. Chem. Phys.* **2015**, *17*, 11516-20. DOI
37. Yin, Y.; Wang, Y.; Li, H.; et al. A flexible dual parameter sensor with hierarchical porous structure for fully decoupled pressure–temperature sensing. *Chem. Eng. J.* **2022**, *430*, 133158. DOI
38. Li, M.; Chen, J.; Zhong, W.; et al. Large-area, wearable, self-powered pressure-temperature sensor based on 3D thermoelectric spacer fabric. *ACS. Sens.* **2020**, *5*, 2545-54. DOI PubMed
39. Zhang, X.; Gong, Y.; Xie, F.; Sun, P.; Jiang, S. Dual-mode temperature-pressure MXene sensor for enhanced firefighter safety and deep learning-enhanced smart gloves. *ACS. Appl. Mater. Interfaces.* **2025**, *17*, 38280-7. DOI PubMed
40. Wang, N.; Xia, Z.; Yang, S.; et al. Pressure-temperature dual-parameter sensors designed by wood-derived thermoelectric composites: micro-pressure high sensitivity. *Compos. Part. B. Eng.* **2023**, *264*, 110928. DOI
41. Wang, Y.; Wu, H.; Xu, L.; Zhang, H.; Yang, Y.; Wang, Z. L. Hierarchically patterned self-powered sensors for multifunctional tactile sensing. *Sci. Adv.* **2020**, *6*, eabb9083. DOI PubMed PMC
42. Desisto, W. J.; Cashon, R.; Cassidy, D.; et al. Preparation and characterization of a selective nitric oxide adsorbent based on Cobalt(II) phthalocyanine tetrasulfonic acid. *Ind. Eng. Chem. Res.* **2008**, *47*, 7857-61. DOI
43. Jo, Y. M.; Jo, Y. K.; Lee, J. H.; Jang, H. W.; Hwang, I. S.; Yoo, D. J. MOF-based chemiresistive gas sensors: toward new functionalities. *Adv. Mater.* **2023**, *35*, e2206842. DOI PubMed
44. Xu, S.; Liu, X.; Wu, J.; Wu, J. NO_x sensor constructed from conductive metal-organic framework and graphene for airway inflammation screening. *ACS. Sens.* **2023**, *8*, 2348-58. DOI PubMed
45. Chang, Y.; Chen, M.; Fu, Z.; et al. Building porphyrin-based MOFs on MXenes for ppb-level NO sensing. *J. Mater. Chem. A.* **2023**, *11*, 6966-77. DOI
46. Pang, Z.; Zhao, Y.; Luo, N.; Chen, D.; Chen, M. Flexible pressure and temperature dual-mode sensor based on buckling carbon nanofibers for respiration pattern recognition. *Sci. Rep.* **2022**, *12*, 17434. DOI PubMed PMC
47. Buist, M.; Bernard, S.; Nguyen, T. V.; Moore, G.; Anderson, J. Association between clinically abnormal observations and subsequent in-hospital mortality: a prospective study. *Resuscitation* **2004**, *62*, 137-41. DOI PubMed

48. Flenady, T.; Dwyer, T.; Applegarth, J. Accurate respiratory rates count: so should you! *Australas. Emerg. Nurs. J.* **2017**, *20*, 45-7. DOI PubMed
49. Borst, C.; Wieling, W.; van Brederode, J. F.; Hond, A.; de Rijk, L. G.; Dunning, A. J. Mechanisms of initial heart rate response to postural change. *Am. J. Physiol.* **1982**, *243*, H676-81. DOI PubMed
50. Weckenmann, M. [The pulse-respiratory quotient of persons with stable and instable postural circulation while standing (author's transl)]. *Basic. Res. Cardiol.* **1975**, *70*, 339-49. DOI PubMed
51. von Bonin, D.; Grote, V.; Buri, C.; et al. Adaption of cardio-respiratory balance during day-rest compared to deep sleep - an indicator for quality of life? *Psychiatry. Res.* **2014**, *219*, 638-44. DOI PubMed
52. Zhang, C.; Zong, P.; Ge, Z.; et al. MXene-based wearable thermoelectric respiration sensor. *Nano. Energy.* **2023**, *118*, 109037. DOI
53. Chen, X.; Zhang, H.; Li, Z.; Liu, S.; Zhou, Y. Continuous monitoring of heart rate variability and respiration for the remote diagnosis of chronic obstructive pulmonary disease: prospective observational study. *JMIR. Mhealth. Uhealth.* **2024**, *12*, e56226. DOI PubMed PMC
54. Kesten, S.; Maleki-Yazdi, R.; Sanders, B. R.; et al. Respiratory rate during acute asthma. *Chest* **1990**, *97*, 58-62. DOI PubMed
55. Huffaker, M. F.; Carchia, M.; Harris, B. U.; et al. Passive nocturnal physiologic monitoring enables early detection of exacerbations in children with asthma. A proof-of-concept study. *Am. J. Respir. Crit. Care. Med.* **2018**, *198*, 320-8. DOI PubMed PMC
56. Dweik, R. A.; Boggs, P. B.; Erzurum, S. C.; et al.; American Thoracic Society Committee on Interpretation of Exhaled Nitric Oxide Levels (FENO) for Clinical Applications. An official ATS clinical practice guideline: interpretation of exhaled nitric oxide levels (FENO) for clinical applications. *Am. J. Respir. Crit. Care. Med.* **2011**, *184*, 602-15. DOI PubMed PMC
57. Jeppegaard, M.; Veidal, S.; Sverrild, A.; Backer, V.; Porsbjerg, C. Validation of ATS clinical practice guideline cut-points for FeNO in asthma. *Respir. Med.* **2018**, *144*, 22-9. DOI PubMed
58. Rupani, H.; Kent, B. D. Using fractional exhaled nitric oxide measurement in clinical asthma management. *Chest* **2022**, *161*, 906-17. DOI PubMed
59. Liu, X.; Zhang, H.; Wang, Y.; et al. Fractional exhaled nitric oxide is associated with the severity of stable COPD. *COPD* **2020**, *17*, 121-7. DOI PubMed
60. Alcázar-Navarrete, B.; Ruiz Rodríguez, O.; Conde Baena, P.; Romero Palacios, P. J.; Agusti, A. Persistently elevated exhaled nitric oxide fraction is associated with increased risk of exacerbation in COPD. *Eur. Respir. J.* **2018**, *51*, 1701457. DOI PubMed